nature materials

ARTICLES

PUBLISHED ONLINE: 17 AUGUST 2015 | DOI: 10.1038/NMAT4369

# Design principles for solid-state lithium superionic conductors

Yan Wang[1], William Davidson Richards[1], Shyue Ping Ong[1,2], Lincoln J. Miara[3], Jae Chul Kim[1], Yifei Mo[1,4] and Gerbrand Ceder[1,5,6]*

**Lithium solid electrolytes can potentially address two key limitations of the organic electrolytes used in today's lithium-ion batteries, namely, their flammability and limited electrochemical stability. However, achieving a $Li^+$ conductivity in the solid state comparable to existing liquid electrolytes (>1 mS cm$^{-1}$) is particularly challenging. In this work, we reveal a fundamental relationship between anion packing and ionic transport in fast Li-conducting materials and expose the desirable structural attributes of good Li-ion conductors. We find that an underlying body-centred cubic-like anion framework, which allows direct Li hops between adjacent tetrahedral sites, is most desirable for achieving high ionic conductivity, and that indeed this anion arrangement is present in several known fast Li-conducting materials and other fast ion conductors. These findings provide important insight towards the understanding of ionic transport in Li-ion conductors and serve as design principles for future discovery and design of improved electrolytes for Li-ion batteries.**

Safety issues are of immense concern in developing advanced energy storage technologies, especially for Li-ion batteries. Commercial Li-ion batteries contain flammable organic liquid electrolyte that poses major technical challenges; most recent major incidents of Li-ion battery fires were caused by ignition of the electrolyte[1,2]. Replacing the organic liquid electrolyte with a solid-state ionic conductor would improve device safety tremendously and remove one of the few remaining barriers to even wider scale use of Li-ion technology. Inorganic solid-state Li-ion conductors also benefit from many other advantages such as superior electrochemical, mechanical and thermal stability, absence of leakage, and the possibility of battery miniaturization[3]. Indeed, solid-state batteries that retain almost full storage capacity over thousands of cycles have been demonstrated[4,5].

Li-ion solid-state conductors require high ionic conductivity at room temperature and low activation energy ($E_a$) for use over a broad range of operating temperatures. In addition, other properties such as electrochemical stability against the anode and cathode, and environmental stability are preferred as they reduce the complexity of the battery. Studies in the past decades have focused mainly on ionically conducting oxides in the LISICON (ref. 6; for example, $Li_{14}ZnGe_4O_{16}$), NASICON (ref. 7; for example, $Li_{1.3}Al_{0.3}Ti_{1.7}(PO_4)_3$), perovskite[8] (for example, $La_{0.5}Li_{0.5}TiO_3$), garnet[9] (for example, $Li_7La_3Zr_2O_{12}$) and LiPON (ref. 10; for example, $Li_{2.88}PO_{3.73}N_{0.14}$) systems. These conductors exhibit ionic conductivities at room temperature of the order of $10^{-3}$ to 1 mS cm$^{-1}$ with $E_a$ ranging from 0.3 to 0.6 eV (ref. 3). Significant progress has been made recently with the discovery of numerous sulphide-based compounds with higher ionic conductivities. Examples of these include the thio-LISICON conductor $Li_{3.25}Ge_{0.25}P_{0.75}S_4$ (2.2 mS cm$^{-1}$ at room temperature, $E_a = 0.22$ eV; ref. 11), $Li_7P_3S_{11}$, a high-conductivity crystalline phase in the $Li_2S$-$P_2S_5$ system (17 mS cm$^{-1}$ at room temperature, $E_a = 0.18$ eV; refs 12,13), and a new member of the thio-LISICON family, $Li_{10}GeP_2S_{12}$ (12 mS cm$^{-1}$ at room temperature, $E_a = 0.22$–$0.25$ eV (refs 14,15). Replacing Ge in $Li_{10}GeP_2S_{12}$ by Sn or Si has been shown to also give a high conductivity with similar activation energy[16–20]. These materials have superior ionic conductivities, comparable to those of liquid electrolytes, making the commercialization of high-performance solid-state Li-ion batteries very promising.

The discovery of new Li-ion conductors has largely proceeded by extending known superionic compounds into new compositional spaces. In this paper we present systematically the attributes of compounds that lead to high Li-ion conductivity, thereby developing specific criteria by which to look for better conductors. We find that the topology of the particular anion arrangement is the key factor in determining intrinsic Li-ion mobility. A body-centred cubic (bcc) anion sublattice allows the lowest activation barrier and highest ionic conductivity, but this is a rare feature in known materials. Our findings explain the observed conductivity trends in known Li-ion conductors, and can be used to design new ionic high-performance materials.

The basic step in ionic diffusion is the migration of the ion between stable sites through a higher energy environment. The highest energy along this path is the activation energy for migration, which in good ionic conductors contributes the main component to the activation energy for long-range diffusion. The stable site for Li in ionic materials is usually a tetrahedral or octahedral site connected to other polyhedral sites in the structure through shared anion triangles. Examples of such paths in common battery cathode materials such as spinel oxides or rocksalt-type oxides are well established[21,22]. To understand the topology of sites in good Li-ion conductors we begin by examining the crystal structure of two compounds having the highest Li-ion conductivity reported so far, $Li_{10}GeP_2S_{12}$ (refs 14,15) and $Li_7P_3S_{11}$ (refs 12,13). The structure of $Li_{10}GeP_2S_{12}$ can be characterized by predominantly tetrahedral coordination of Li, Ge and P cations within a tetragonal lattice[14,23]. In the structure of $Li_7P_3S_{11}$, corner-sharing $P_2S_7^{4-}$ ditetrahedra

[1]Department of Materials Science and Engineering, Massachusetts Institute of Technology, Cambridge, Massachusetts 02139, USA. [2]Department of NanoEngineering, University of California, San Diego, La Jolla, California 92093, USA. [3]Samsung Advanced Institute of Technology-USA, 1 Cambridge Center, Suite 702, Cambridge, Massachusetts 02142, USA. [4]Department of Materials Science and Engineering, University of Maryland, College Park, Maryland 20742, USA. [5]Department of Materials Science and Engineering, University of California, Berkeley, California 94720, USA. [6]Materials Sciences Division, Lawrence Berkeley National Laboratory, Berkeley, California 94720, USA. *e-mail: gceder@berkeley.edu

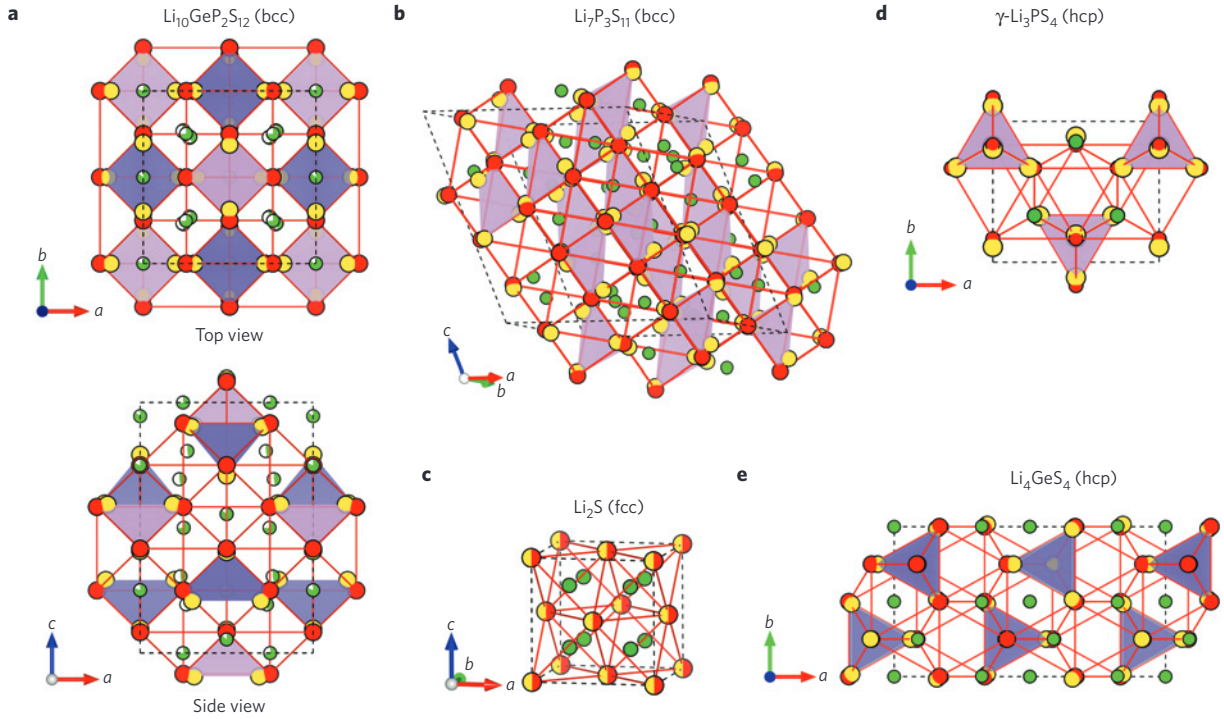


**Figure 1 | Mapping of the anion sublattice to a bcc/fcc/hcp framework in solid-state Li-ion conductors. a–e**, Crystal structure of Li-ion conductors $Li_{10}GeP_2S_{12}$ (**a**), $Li_7P_3S_{11}$ (**b**), $Li_2S$ (**c**), -$Li_3PS_4$ (**d**) and $Li_4GeS_4$ (**e**). Li atom, partially occupied Li atom, S atom, $PS_4$ tetrahedra and $GeS_4$ tetrahedra (partially occupied in $Li_{10}GeP_2S_{12}$) are coloured green, green–white, yellow, purple and blue, respectively. In both $Li_{10}GeP_2S_{12}$ and $Li_7P_3S_{11}$, the sulphur anion sublattice can be closely mapped to a bcc framework (red circles connected by red lines). In $Li_2S$, the anion sublattice is an exact fcc matrix (yellow–red circles). The anion sublattices in -$Li_3PS_4$ and $Li_4GeS_4$ are closely matched to a hcp framework.

and $PS_4^{3-}$ tetrahedra are surrounded by Li ions primarily having tetrahedral coordination[12]. To abstract and understand the anion arrangements in these structures better, we apply a structure matching algorithm to map the sulphur positions to the three most common crystal lattices: bcc, face-centred cubic (fcc) and hexagonal close-packed (hcp) lattices. Despite seeming to be very different structures, we find that the sulphur sublattices of both $Li_{10}GeP_2S_{12}$ and $Li_7P_3S_{11}$ very closely match a bcc lattice. The matchings are graphically shown in Fig. 1a,b, with details of the algorithm and the matching results given in Methods, Supplementary Fig. 1 and Supplementary Table 1.

To explain the predominance of bcc sulphur frameworks in high-conductivity solid electrolytes, we compare the calculated $Li^+$ migration barrier within the bcc, fcc and hcp $S^{2-}$ anion lattices in the dilute limit of a single $Li^+$ in a fixed $S^{2-}$ lattice with no other cations present. This computational experiment allows us to directly assess the effect of the anion configuration. The fcc and hcp lattices are present in many lithium sulphide materials. For example, $Li_2S$ has an fcc sulphur sublattice (Fig. 1c); $Li_4GeS_4$ and -$Li_3PS_4$ (space group: $Pmn2_1$), the parent structures of $Li_{10}GeP_2S_{12}$ and other thio-LISICONs, both have an hcp sulphur sublattice (Fig. 1d,e). We use a lattice volume of 40 $Å^3$ per S atom (the same as $Li_{10}GeP_2S_{12}$) to keep the same free volume for Li diffusion in all anion lattices. The migration paths and their energy are shown in Fig. 2.

We find that for all S lattices Li is most stable in the tetrahedral site. In the bcc $S^{2-}$ lattice, the Li ion migrates with a remarkably low barrier of only 0.15 eV along a path connecting two face-sharing tetrahedral sites (T1 and T2 in Fig. 2a), hereafter denoted as the T–T path. In the fcc anion lattice, Li migration between two tetrahedral sites (T1 and T2 in Fig. 2b) is through an intermediate octahedral site (O1), hereafter denoted as the T–O–T path. This path is similar to what has been documented in fcc-structured oxides[21,24]. The presence of the octahedral site along the path makes the barrier for T–O–T type migration in fcc much higher (0.39 eV at this volume). The T–O–T type path can be also found in the *a*–*b* plane of the hcp lattice (T1 to T2 through O1 in Fig. 2c) with an almost identical activation barrier (0.40 eV). Li migration along the *c* axis of the hcp lattice is primarily through a path connecting two face-sharing tetrahedral sites (T1 and T3) with a lower barrier (0.20 eV), but it does not percolate and requires Li migration through octahedral sites to achieve long-range Li diffusion. Li could also migrate between face-sharing octahedral sites (O1 and O2, 0.19 eV) along the *c* axis; however, additional activation energy is required to access this path as the octahedral sites are unstable. Therefore, Li conduction in a hcp lattice is likely to occur by an alternation of T–T and T–O–T hopping, and the T–O–T hops, with higher energy barriers, are the rate-limiting steps. At room temperature this difference in activation energies between the bcc T–T path and hcp/fcc T–O–T paths corresponds to about three orders of magnitude difference in conductivity ( ), according to the relation $\exp(-E_a/kT)$.

Volume is thought to be an important factor in ion mobility[16]. We extend our analysis by evaluating the previously discussed migration barriers in all three lattices as a function of volume between 28.5 $Å^3$ and 70.8 $Å^3$ (per S atom), which is the range observed in the inorganic crystal structure database[25] (ICSD) for compounds that contain Li and S but not N, O, Se, F, Cl, Br, I or H (Supplementary Fig. 2). We find that for the bcc lattice the tetrahedral site is lowest in energy for all volumes (Supplementary Fig. 3 and Supplementary Table 2), with the Li migration barrier monotonically decreasing as volume increases. The bcc arrangement remains optimal for Li mobility across all volumes (Fig. 3). In fcc and hcp lattices the Li migration mechanism varies with the lattice volume. At small volumes (regime I in Fig. 3), the most stable Li sites are octahedral owing to the larger size of this site and the activation barrier is very large owing to a large energy penalty when the Li ion passes through an extremely small three-coordinated bottleneck.

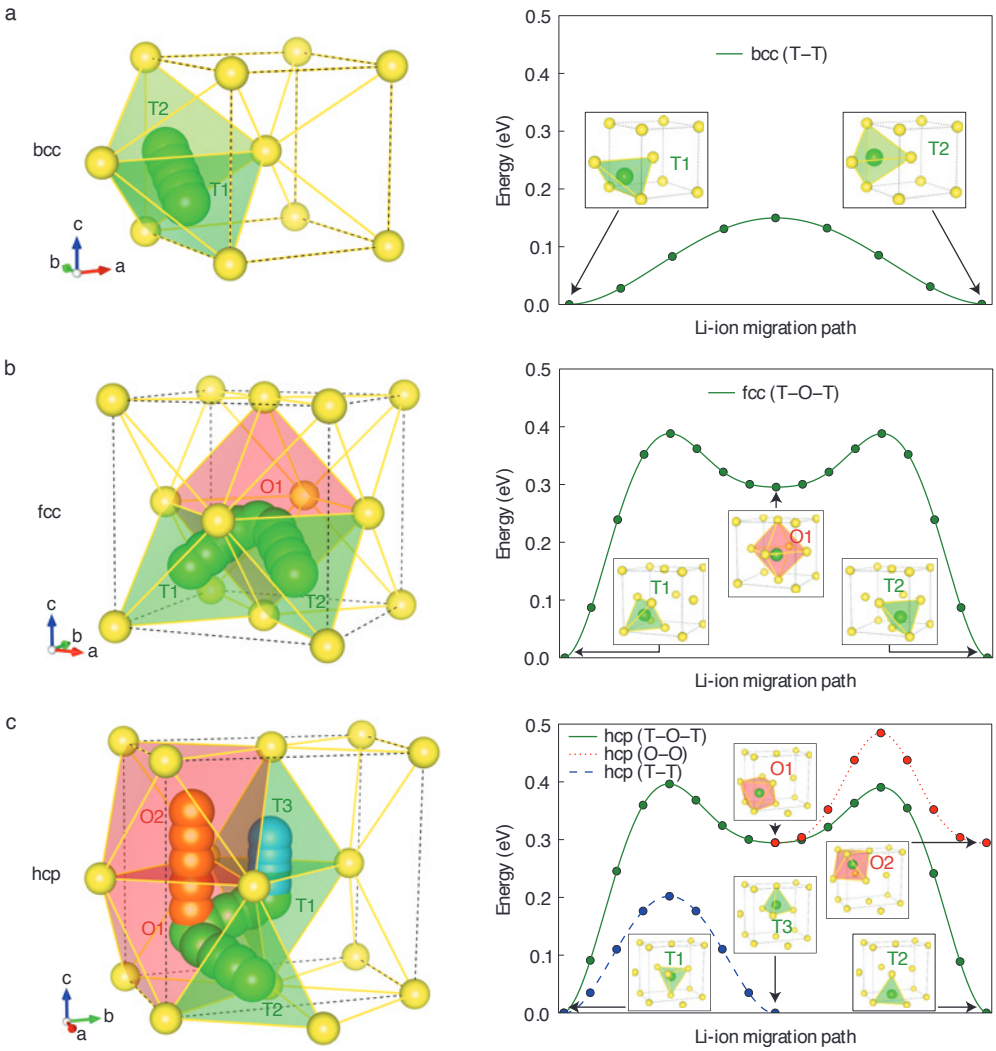


**Figure 2 | Li-ion migration pathways in bcc/fcc/hcp-type anion lattices. a–c**, Li-ion migration path (left panels) and calculated energy path (right panels) in bcc (**a**), fcc (**b**) and hcp (**c**) sulphur lattices. The sulphur anions are coloured yellow, and the Li ions are coloured green, blue and red for di erent paths. $LiS_4$ tetrahedra and $LiS_6$ octahedra are coloured green and red, respectively.

As the volume gets larger (regime II in Fig. 3), the tetrahedral site becomes more stable, and the activation energy decreases as the size of the three-coordinated bottleneck increases. The crossover in site energies creates non-monotonic behaviour of the migration energy with volume in these close-packed lattices. At larger volumes (regime III in Fig. 3), the octahedral site is no longer stable, and Li migration occurs directly between two tetrahedral sites bypassing the centre of the octahedra, with a decreasing barrier as the volume further increases. The detailed results for the energy path of Li-ion migration in structures with different volumes are shown in Supplementary Figs 4–6. The results in Fig. 3 indicate clearly that bcc is the preferred anion arrangement for Li-ion conductors owing to the low barrier of the T–T path.

The above model analysis is validated by comparing it to the experimental activation energy in real compounds. The calculated 0.15 eV barrier in the bcc sulphur lattice with a volume of 40 Å$^3$ is only slightly lower than the experimentally determined activation energies of $Li_{10}GeP_2S_{12}$ (0.25 eV (ref. 14) and 0.22 eV (ref. 15)) and other derivatives with similar structures (0.22 eV of $Li_7GePS_8$ (ref. 15), 0.20 eV of $Li_{10}SiP_2S_{12}$ (ref. 19) and 0.27 eV of $Li_{10}SnP_2S_{12}$ (refs 17,18)), and very close to that of $Li_7P_3S_{11}$ (0.18 eV; ref. 13) with a similar volume (37.7 Å$^3$), as shown in Fig. 3. The experimental activation energies of $Li_4GeS_4$ (0.53 eV

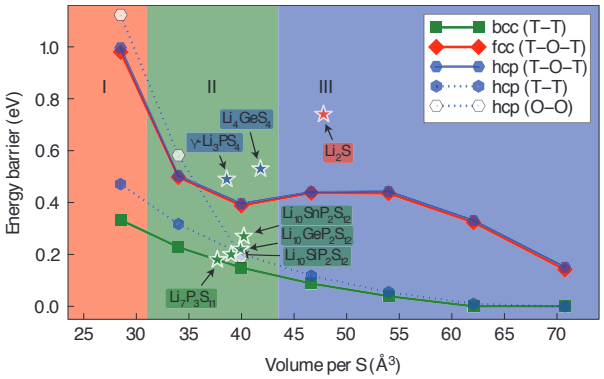


**Figure 3 | Activation barrier for Li-ion migration versus lattice volume.** Activation barrier calculated for the Li-ion migration pathways in the bcc/fcc/hcp $S^{2-}$ lattices at di erent volumes. Solid and dotted lines are guides to the eye. Experimental activation energies for $Li_{10}GeP_2S_{12}$ (ref. 15), $Li_{10}SnP_2S_{12}$ (refs 17,18), $Li_{10}SiP_2S_{12}$ (ref. 19), $Li_7P_3S_{11}$ (ref. 13), $Li_2S$ (ref. 42), $Li_4GeS_4$ (ref. 26) and -$Li_3PS_4$ (ref. 26) are marked by a star symbol for comparison. The underestimate of the activation energy for $Li_2S$ is due to fact that the experimental value contains contributions from the defect formation energy.

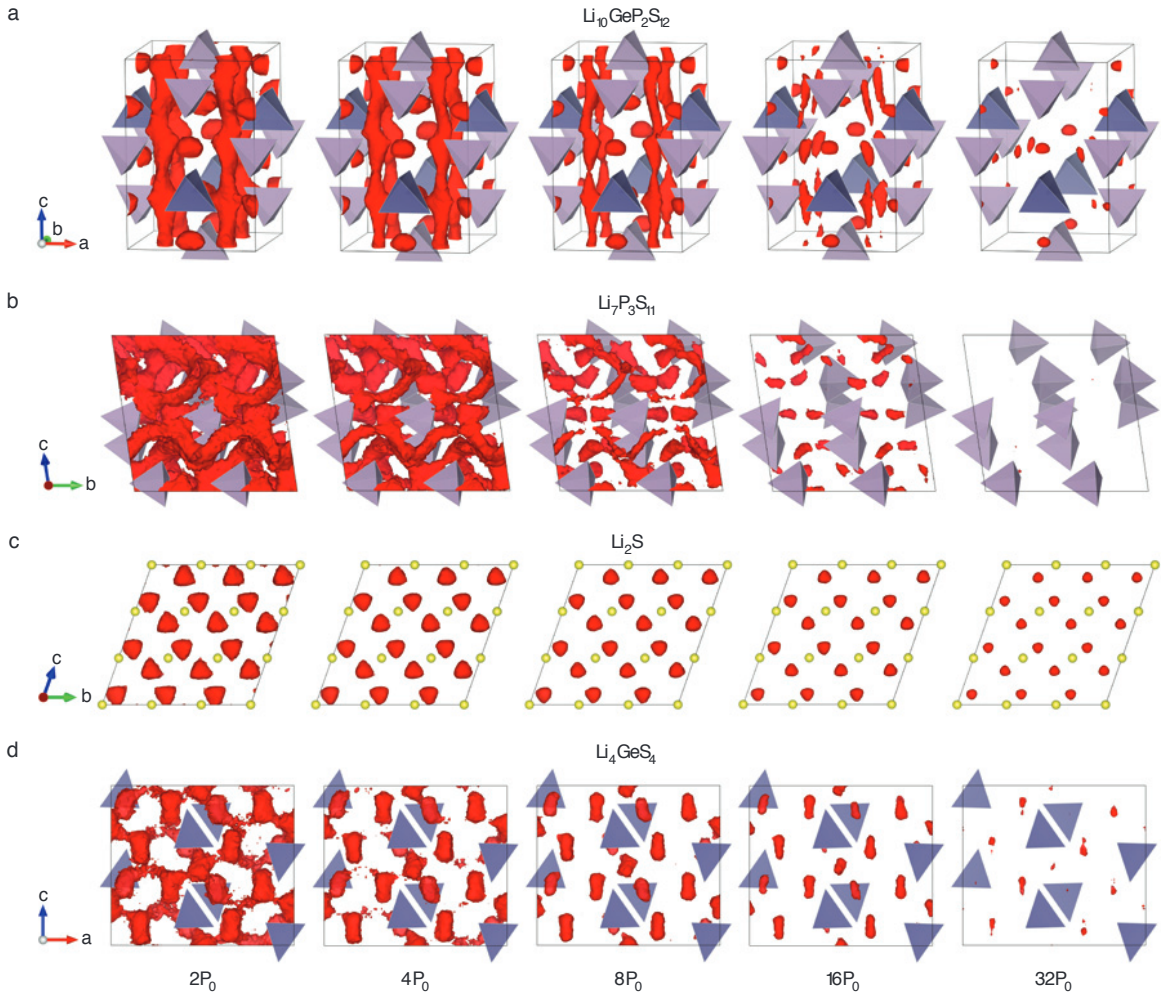


**Figure 4 | Li-ion probability densities in Li-ion conductors. a–d**, The probability densities of Li ions are obtained from ab initio molecular dynamics simulations at 900 K in $Li_{10}GeP_2S_{12}$ (**a**), $Li_7P_3S_{11}$ (**b**), $Li_2S$ (**c**) and $Li_4GeS_4$ (**d**). Isosurfaces of the ionic probability densities are plotted at increasing isovalues ranging from $2P_0$ to $32P_0$, in which $P_0$ is defined as the mean value of the density for each structure. $PS_4$ tetrahedra and $GeS_4$ tetrahedra are coloured purple and blue, respectively. The sulphur atoms are shown as small yellow circles for $Li_2S$.

(ref. 26) with a volume of 41.8 Å$^3$) and -$Li_3PS_4$ (0.49 eV (ref. 26) with a volume of 38.6 Å$^3$) are also close to the calculated barrier for the hcp lattice (0.40 eV at $V = 40.0$ Å$^3$). It is to be expected that the barriers for real compounds are higher than those in our model analysis, as the electrostatic interaction between the migrating $Li^+$ and the other cations is usually the highest in the activated state[24,27], so adding the relevant cations in our simulations would increase activation energies. For structures without any tetrahedral vacancies such as $Li_2S$, our model underpredicts the diffusion activation energy as it considers only the migration barrier and not the contribution of the defect (for example, vacancy) formation energy.

Our analysis of differences in the diffusion mechanisms of bcc, fcc and hcp sulphur lattices is further confirmed by the probability density of Li ions obtained from *ab initio* molecular dynamics simulations for several Li-ion conductors (Fig. 4). The simulations are performed at 900 K to speed up diffusion and reduce the simulation time. The probability density is defined as the time-averaged spatial occupancy probability of Li ions in the crystal structure, and is inversely correlated to the Li site energy. For two sites with probabilities $P_1$ and $P_2$, the difference in their free energies can be given approximately by $G = -kT\ln(P_1/P_2)$. At 900 K, each doubling of probability corresponds to a decrease in Li site energy of about 50 meV.

The distribution of Li ions in $Li_{10}GeP_2S_{12}$ demonstrates that conduction occurs predominantly via the channels connecting tetrahedrally coordinated Li sites along the *c* axis (Fig. 4a). Notably, the probability density extends between these tetrahedral sites with relatively large probabilities, suggesting high Li occupancy along the diffusion channels, which is also seen experimentally[14,28]. The evenly distributed probability densities indicate that Li ions have a relatively flat energy landscape along the channels, and the energy barriers for diffusion between these sites are low, in agreement with our analysis of the bare sulphide lattices. In $Li_7P_3S_{11}$ the probability densities form a three-dimensional Li diffusion network (Fig. 4b). As compared with $Li_{10}GeP_2S_{12}$, the densities in $Li_7P_3S_{11}$ are more evenly distributed within the diffusion network, confirming the small activation energy of 0.18 eV (0.19 eV) reported experimentally[13] (computationally, Supplementary Fig. 7), even lower than that of $Li_{10}GeP_2S_{12}$ (0.22 0.25 eV; refs 14,15). In contrast, Li ions are almost exclusively found on the isolated tetrahedral sites in the fcc sulphur framework of $Li_2S$ (Fig. 4c) even when Li vacancies are induced (see Methods). The Li occupancy is negligibly small at the octahedral sites, which are required to connect the tetrahedral sites and form a percolating diffusion network. The absence of a connected diffusion network indicates that the Li ions hop through these octahedral sites at a very low frequency, and that the octahedral site energies are much higher

than in the tetrahedral sites, again in agreement with the results on the bare sulphide lattices. In $Li_4GeS_4$, which has an underlying hcp sulphur lattice, the probability densities are localized in pairs of face-sharing tetrahedral sites (elliptical regions in Fig. 4d), corresponding to the T–T path (Fig. 2c). A percolation network for long-range Li diffusion can be formed only through the bridging octahedral sites, which have significantly smaller occupation probability. Therefore, the energy landscape for Li ions in $Li_4GeS_4$ and $Li_2S$ is considerably more corrugated than in $Li_{10}GeP_2S_{12}$ or $Li_7P_3S_{11}$, leading to the higher activation energies found in $Li_4GeS_4$ and $Li_2S$.

A general principle for the design of Li-ion conductors with low activation energy can be distilled from the above findings: all of the sites within the diffusion network should be energetically close to equivalent, with large channels connecting them. The superior ionic conductivity of Li-ion conductors with a bcc-like anion framework, for example, $Li_{10}GeP_2S_{12}$ and $Li_7P_3S_{11}$, is due to the primarily tetrahedral coordination of the Li ions and their geometric similarity to the bcc anion sublattice, which contains a percolating network composed entirely of tetrahedral sites that are crystallographically and energetically equivalent. This is unlike structures with the more common hcp or fcc anion frameworks, which require migration through sites with very different coordination (for example, 4 and 6) to achieve percolation.

In Fig. 5 we show the Li-containing sulphides from ICSD screened with our bcc framework matching algorithm. Transition-metal-containing compounds are excluded as transition-metal cations can be easily reduced against the lithium anode. Only 25 compounds can be matched to bcc, and most of them are significantly distorted from a perfect bcc lattice. The superionic conductors $Li_{10}GeP_2S_{12}$ and $Li_7P_3S_{11}$ are among the few sulphides that are well matched to bcc. This screening demonstrates that the bcc framework serves as a descriptor for Li-ion conductors with high conductivity. A few other Li-ion conductors, such as $Li_3BS_3$ (ref. 29) and -$Li_3PS_4$ (space group: *Pnma*)[30,31], which are reported to exhibit high conductivities and low activation energies, also emerge from this screening. Note that the screening results include materials whose closest match is hcp or fcc sublattice (for example, -$Li_3PS_4$ and $Li_4GeS_4$, see Methods) but that can be mapped to bcc if relatively large length and angle deviations are allowed. As the bcc framework is much less common for anions than hcp or fcc, very high ionic conductivity is limited to a small group of compounds.

We expect the above principle to be transferable to other combinations of mobile cations and immobile anion lattices. For example, in the recently discovered Li-ion conductors $Li_3OCl$ and $Li_3OBr$ with the anti-perovskite structure[32] the oxygen and halide anions are bcc packed. With the presence of Li interstitials the activation energy can be as low as 0.17 eV as they activate a path connecting energy-equivalent tetrahedral sites[33]. The known fast $Ag^+$ and $Cu^+$ conducting halides and chalcogenides (for example, -AgI) also have bcc anion sublattices, and possess higher ionic conductivities than fcc and hcp-based phases[34]. Consistent with these findings, our calculations indicate that in lattices formed by $O^{2-}$ or halide anions (for example, $Br^-$), the Li migration barrier in bcc-type anion frameworks is also lower than that of other close-packed types (Supplementary Figs 8 and 9). Moreover, we find that a bcc anion sublattice is also superior for $Na^+$ or $Mg^{2+}$ ion migration than the other close-packed types (Supplementary Figs 10 and 11), and such information could be useful for the design of sodium and multivalent solid-state battery systems[35]. We note that although we predict low activation energies for oxides with bcc oxygen framework (Supplementary Fig. 8), the typically higher activation energy one finds in oxides mainly comes from the much lower frequency with which oxygen takes on a bcc-like arrangement compared with sulphur, and from the smaller volume and reduced polarizability of oxides, which increases the electrostatic interactions between the migrating ion and the other cations.

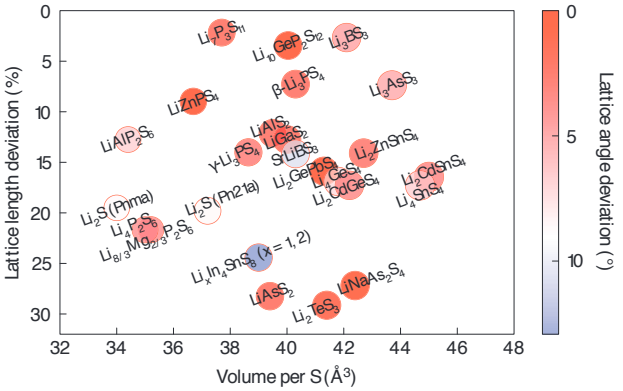


**Figure 5 | Similarity of screened ICSD structures containing Li and S to a bcc anion framework using the structural matching algorithm.** Compounds with transition-metal cations are excluded. The lattice length deviation is defined as $_l = 1 - \min(a,b,c)/\max(a,b,c)$, and the angle deviation is defined as $ = \max(|90 - |, |90 - |, |90 - |)$, where $a$, $b$, $c$, , and are the conventional unit-cell parameters of the transformed lattice (see Methods and Supplementary Fig. 1). For an ideal compound with a perfect bcc anion framework $_l = = 0$.

It is worth noting that there exist a few examples of non-bcc-type anion frameworks that also accommodate a network composed entirely of tetrahedral sites for the mobile cations. Such frameworks can be found in the crystal structures of ionic conductors including the argyrodite-type $Li_7PS_6$ and its halide-substituted derivatives $Li_6PS_5X$ (X = Cl, Br, I; ref. 36), and a very recently reported sodium conductor cubic-$Na_3PS_4$ (refs 37,38), which exhibit good ionic conductivities close to 1 mS cm$^{-1}$ at room temperature. These structures' frameworks cannot be closely matched to a bcc, fcc or hcp sublattice, but the underlying mechanism for cation migration through the percolating face-shared tetrahedral sites with low activation energy is fundamentally very similar to the bcc-type superionic conductors.

Whereas the underlying anion sublattice dominates the activation energy by setting the site connectivity, the presence of the other lithium and non-lithium cations will modify the migration energy from what can be achieved in the bare lattice. When multiple non-Li cations share the same type of site in the crystal structure (for example, Ge/P in $Li_{10}GeP_2S_{12}$), they can locally modify the energy landscape, creating additional barriers. Preferential attraction of Li ions or vacancies to one of the metal cations is a manifestation of this. Hence, doping is ideally done with cations that are close to each other in the periodic table and chemically similar. This local cation effect can also be used as an advantage by appropriately engineering site energies in a structure to reduce the energy difference between Li occupation in different sites. For example, we found that[16] the substitution of Si for Ge (an element closer to P in the periodic table) in $Li_{10}GeP_2S_{12}$ lowers its activation energy by 0.01 eV (confirmed by experiment[19], 0.05 eV lower), and replacing Ge with Sn (less similar to P) increases it by 0.03 eV (confirmed by experiment[18], 0.02 eV higher). The changes in activation energy can be explained by the changes in Li site energies associated with the cation substitution (Supplementary Fig. 12). In addition, one may tailor the ionic conduction mechanism and conductivity by changing the Li concentration. In garnet-type $Li_xLa_3M_2O_{12}$ ($M$ denotes various metallic or metalloid cations) ionic conductors, it is found that as the Li concentration increases from $x = 3$ to $x = 7$, the limited number of tetrahedral sites and the electrostatic repulsion among Li ions force the Li ions to the higher energy octahedral sites[39]. This eliminates the large energy difference between the tetrahedral and octahedral site, resulting in a lower activation energy and higher Li conductivity[40,41].

In summary, our study highlights the critical influences of the anion-host matrix on the ionic conductivity of solid-state Li-ion conductors. A new descriptor emerges from our findings: anion sublattices with bcc-like frameworks are superior for Li-ion diffusion leading to a lower activation barrier than in other close-packed frameworks. The bcc anion framework allows the Li ions to migrate within a network of interconnected tetrahedral sites possessing equivalent energies. This feature is found in recently synthesized superionic Li-ion conductors such as $Li_{10}GeP_2S_{12}$ and $Li_7P_3S_{11}$. These new insights have predictive power and can serve as valuable design guidelines for developing fast ion-conducting materials with improved properties, as well as for further searches for new types of Li-ion conductor material.

## Methods

Methods and any associated references are available in the online version of the paper.

Received 5 March 2015; accepted 25 June 2015; published online 17 August 2015

## References


1. Gallagher, S. Boeing's Dreamliner batteries 'inherently unsafe'—and yours may be too. *Ars Technica* (January, 2013); http://arstechnica.com/business/2013/01/boeings-dreamliner-batteries-inherently-unsafe-and-yours-may-be-too
2. Meier, F. & Woodyard, C. Feds review third Tesla fire as shares fall again. *USA Today* (7 November 2013); http://www.usatoday.com/story/money/cars/2013/11/07/third-fire-in-tesla-model-s-reported/3465717
3. Knauth, P. Inorganic solid Li ion conductors: An overview. *Solid State Ion.* **180**, 911–916 (2009).
4. Bates, J. B., Dudney, N. J., Neudecker, B., Ueda, A. & Evans, C. D. Thin-film lithium and lithium-ion batteries. *Solid State Ion.* **135**, 33–45 (2000).
5. Li, J., Ma, C., Chi, M., Liang, C. & Dudney, N. J. Solid electrolyte: The key for high-voltage lithium batteries. *Adv. Energy Mater.* **5**, 1401408 (2015).
6. Bruce, P. G. The A-C conductivity of polycrystalline LISICON, $Li_{2+2x}Zn_{1-x}GeO_4$, and a model for intergranular constriction resistances. *J. Electrochem. Soc.* **130**, 662–669 (1983).
7. Aono, H. Ionic conductivity of solid electrolytes based on lithium titanium phosphate. *J. Electrochem. Soc.* **137**, 1023–1027 (1990).
8. Inaguma, Y. *et al.* High ionic conductivity in lithium lanthanum titanate. *Solid State Commun.* **86**, 689–693 (1993).
9. Murugan, R., Thangadurai, V. & Weppner, W. Fast lithium ion conduction in garnet-type $Li_7La_3Zr_2O_{12}$. *Angew. Chem. Int. Ed.* **46**, 7778–7781 (2007).
10. Yu, X., Bates, J. B., Jellison, G. E. Jr & Hart, F. X. A stable thin-film lithium electrolyte: Lithium phosphorus oxynitride. *J. Electrochem. Soc.* **144**, 524–532 (1997).
11. Kanno, R. & Murayama, M. Lithium ionic conductor thio-LISICON: The $Li_2S$–$GeS_2$–$P_2S_5$ system. *J. Electrochem. Soc.* **148**, A742 (2001).
12. Yamane, H. *et al.* Crystal structure of a superionic conductor, $Li_7P_3S_{11}$. *Solid State Ion.* **178**, 1163–1167 (2007).
13. Seino, Y., Ota, T., Takada, K., Hayashi, A. & Tatsumisago, M. A sulphide lithium super ion conductor is superior to liquid ion conductors for use in rechargeable batteries. *Energy Environ. Sci.* **7**, 627–631 (2014).
14. Kamaya, N. *et al.* A lithium superionic conductor. *Nature Mater.* **10**, 682–686 (2011).
15. Kuhn, A., Duppel, V. & Lotsch, B. V. Tetragonal $Li_{10}GeP_2S_{12}$ and $Li_7GePS_8$—exploring the Li ion dynamics in LGPS Li electrolytes. *Energy Environ. Sci.* **6**, 3548–3552 (2013).
16. Ong, S. P. *et al.* Phase stability, electrochemical stability and ionic conductivity of the $Li_{10}\pm$ 1MP2X12 (M = Ge, Si, Sn, Al or P, and X = O, S or Se) family of superionic conductors. *Energy Environ. Sci.* **6**, 148–156 (2013).
17. Bron, P. *et al.* $Li_{10}SnP_2S_{12}$: An affordable lithium superionic conductor. *J. Am. Chem. Soc.* **135**, 15694–15697 (2013).
18. Kuhn, A. *et al.* A new ultrafast superionic Li-conductor: Ion dynamics in $Li_{11}Si_2PS_{12}$ and comparison with other tetragonal LGPS-type electrolytes. *Phys. Chem. Chem. Phys.* **16**, 14669–14674 (2014).
19. Whiteley, J. M., Woo, J. H., Hu, E., Nam, K.-W. & Lee, S.-H. Empowering the lithium metal battery through a silicon-based superionic conductor. *J. Electrochem. Soc.* **161**, A1812–A1817 (2014).
20. Kato, Y. *et al.* Synthesis, structure and lithium ionic conductivity of solid solutions of $Li_{10}(Ge_{1-x}M_x)P_2S_{12}$ (M = Si, Sn). *J. Power Sources* **271**, 60–64 (2014).
21. Van der Ven, A., Bhattacharya, J. & Belak, A. A. Understanding Li diffusion in Li-intercalation compounds. *Acc. Chem. Res.* **46**, 1216–1225 (2013).
22. Urban, A., Lee, J. & Ceder, G. The configurational space of rocksalt-type oxides for high-capacity lithium battery electrodes. *Adv. Energy Mater.* **4**, 1400478 (2014).
23. Kuhn, A., Köhler, J. & Lotsch, B. V. Single-crystal X-ray structure analysis of the superionic conductor $Li_{10}GeP_2S_{12}$. *Phys. Chem. Chem. Phys.* **15**, 11620–11622 (2013).
24. Kang, K. & Ceder, G. Factors that affect Li mobility in layered lithium transition metal oxides. *Phys. Rev. B* **74**, 094105 (2006).
25. *Inorganic Crystal Structure Database* (FIZ Karlsruhe, 2014); http://icsd.fiz-karlsruhe.de/icsd
26. Murayama, M., Sonoyama, N., Yamada, A. & Kanno, R. Material design of new lithium ionic conductor, thio-LISICON, in the $Li_2S$–$P_2S_5$ system. *Solid State Ion.* **170**, 173–180 (2004).
27. Van der Ven, A., Ceder, G., Asta, M. & Tepesch, P. First-principles theory of ionic diffusion with nondilute carriers. *Phys. Rev. B* **64**, 184307 (2001).
28. Mo, Y., Ong, S. P. & Ceder, G. First principles study of the $Li_{10}GeP_2S_{12}$ lithium super ionic conductor material. *Chem. Mater.* **24**, 15–17 (2012).
29. Vinatier, P., Gravereau, P., Ménétrier, M., Trut, L. & Levasseur, A. $Li_3BS_3$. *Acta Crystallogr. C* **50**, 1180–1183 (1994).
30. Homma, K. *et al.* Crystal structure and phase transitions of the lithium ionic conductor $Li_3PS_4$. *Solid State Ion.* **182**, 53–58 (2011).
31. Liu, Z. *et al.* Anomalous high ionic conductivity of nanoporous -$Li_3PS_4$. *J. Am. Chem. Soc.* **135**, 20–23 (2013).
32. Zhao, Y. & Daemen, L. L. Superionic conductivity in lithium-rich anti-perovskites. *J. Am. Chem. Soc.* **134**, 15042–15047 (2012).
33. Emly, A., Kioupakis, E. & Van der Ven, A. Phase stability and transport mechanisms in antiperovskite $Li_3OCl$ and $Li_3OBr$ superionic conductors. *Chem. Mater.* **25**, 4663–4670 (2013).
34. Hull, S. Superionics: Crystal structures and conduction processes. *Rep. Prog. Phys.* **67**, 1233–1314 (2004).
35. Yoo, H. D. *et al.* Mg rechargeable batteries: An on-going challenge. *Energy Environ. Sci.* **6**, 2265–2279 (2013).
36. Deiseroth, H. J. *et al.* $Li_6PS_5X$: A class of crystalline Li-rich solids with an unusually high $Li^+$ mobility. *Angew. Chem. Int. Ed.* **47**, 755–758 (2008).
37. Hayashi, A., Noi, K., Sakuda, A. & Tatsumisago, M. Superionic glass-ceramic electrolytes for room-temperature rechargeable sodium batteries. *Nature Commun.* **3**, 856 (2012).
38. Tanibata, N. *et al.* X-ray crystal structure analysis of sodium-ion conductivity in $^{94}Na_3PS_4{\cdot}6Na_4SiS_4$ glass-ceramic electrolytes. *ChemElectroChem* **1**, 1130–1132 (2014).
39. Xie, H., Alonso, J. A., Li, Y., Fernández-Díaz, M. T. & Goodenough, J. B. Lithium distribution in aluminum-free cubic $Li_7La_3Zr_2O_{12}$. *Chem. Mater.* **23**, 3587–3589 (2011).
40. Xu, M. *et al.* Mechanisms of $Li^+$ transport in garnet-type cubic $Li_{3+x}La_3M_2O_{12}$ (M = Te, Nb, Zr). *Phys. Rev. B* **85**, 052301 (2012).
41. Miara, L. J. *et al.* Effect of Rb and Ta doping on the ionic conductivity and stability of the garnet $Li_{7+2x-y}(La_{3-x}Rb_x)(Zr_{2-y}Ta_y)O_{12}$ ($0 \le x \le 0.375, 0 \le y \le 1$) superionic conductor: A first principles investigation. *Chem. Mater.* **25**, 3048–3055 (2013).
42. Lin, Z., Liu, Z., Dudney, N. J. & Liang, C. Lithium superionic sulfide cathode for all-solid lithium–sulfur batteries. *ACS Nano* **7**, 2829–2833 (2013).


## Acknowledgements

This work was supported by the Samsung Advanced Institute of Technology. Computational resources from the National Energy Research Scientific Computing Center (NERSC) and from the Extreme Science and Engineering Discovery Environment (XSEDE) are gratefully acknowledged.

## Author contributions

G.C., W.D.R. and Y.W. proposed the concept. Y.W. carried out the calculations and together with W.D.R. prepared the manuscript initially. W.D.R. conceived and implemented the structural matcher algorithm. All authors contributed to the discussions and revisions of the manuscript.

## Additional information

Supplementary information is available in the online version of the paper. Reprints and permissions information is available online at www.nature.com/reprints. Correspondence and requests for materials should be addressed to G.C.

## Competing financial interests

The authors declare no competing financial interests.

## Methods

**Crystal structure analysis.** A structural matching algorithm was used for mapping the anion sublattice structure of Li-ion conductors to a bcc/fcc/hcp framework and implemented in the python materials genomics (pymatgen) open-source library[43]. The algorithm finds all supercell and affine transformations mapping the input bcc, fcc or hcp lattice exactly onto the lattice of the target structure and preserving lattice lengths and angles to within given tolerances. It selects the mapping that minimizes the root-mean-square distance from the atoms in the transformed (and slightly distorted) bcc/fcc/hcp-like supercell structure to the corresponding atoms in the target structure. For the mappings to the bcc lattice presented in Fig. 5, all affine transformations preserving bcc supercell lattice angles to within 5 , and supercell lattice vector lengths to within 20% are considered in the matching, and the maximum allowed r.m.s. is set to be $0.3(V/n)^{1/3}$ for the mapping, where $V/n$ is the normalized volume by number of atoms. With these tolerances, it is possible that a structure matches to more than one framework type, for example allowing the anion lattices of -$Li_3PS_4$ and $Li_4GeS_4$ (close matches to hcp) to match to bcc albeit with relatively large lattice length and angle deviations. For the results shown in Fig. 1, tighter matching tolerances of 3 for supercell lattice angles and 5% for supercell lattice vector lengths are used, ensuring both that structures in Fig. 1 are very closely mapped to their framework type and that they can map to only a single type. An example of matching $Li_{10}GeP_2S_{12}$ to a bcc S lattice can be found in Supplementary Fig. 1. The structural matching results were visualized using VESTA (ref. 44).

**Li-ion migration barrier calculations.** Density functional theory based on the Perdew–Burke–Ernzerhof (PBE) generalized gradient approximation[45] with interactions between ion cores and valence electrons described by the projector augmented wave (PAW) method[46] as implemented in the VASP package[47] was employed in the present work. The VASP pseudopotential set of Li (PAW_PBE Li 17Jan2003), S (PAW_PBE S 17Jan2003), P (PAW_PBE P 17Jan2003), Ge (PAW_PBE Ge 05Jan2001), Si (PAW_PBE Si 05Jan2001) and Sn (PAW_PBE Sn_d 06Sep2000) was used. Activation barriers for a Li ion in sulphur bcc/fcc/hcp lattices were calculated using the climbing-image nudged elastic band method[48] in a large supercell comprising $3 \times 3 \times 3$ conventional unit cells to minimize the interaction between the periodic images. A $2 \times 2 \times 2$ k-point grid was used and the cutoff of the kinetic energy was set to 500 eV for all climbing-image nudged elastic band method calculations. The supercells containing excess electrons were compensated with a uniform background charge. All S atoms were fixed and only the migrating Li atom is allowed to relax. The calculated charge distribution and the Li-ion migration barrier in the $S^{2-}$ supercells with a single $Li^+$ are in good agreement to those from calculations with explicit cations (Supplementary Figs 13–15).

**Li-ion probability density calculations.** The lithium ionic probability densities were calculated from the atom trajectories monitored during the *ab initio* molecular dynamics (AIMD) simulations. The simulations were taken on the canonical ensemble with a time step of 2 fs, with simulations lasting 200 ps for statistical analysis. A gamma-point-only sampling of k-space and a lower plane-wave energy cutoff of 280 eV was used for all AIMD simulations. Details of the AIMD simulation process can be found in previous works[16,28]. The ionic probability density values within a structure were calculated by subdividing the supercell into a grid of cubic cells with an edge length of 0.2 Å and counting the number of time steps for which each cell is occupied by a Li ion. The total ionic probability density $P_i = N/$ , where $N$ is the number of Li ions in the unit cell and is the volume of the unit cell. Li vacancies are introduced in calculations of $Li_2S$ and $Li_4GeS_4$ (6% and 9% of the Li ions are removed from the supercell of $Li_2S$ and $Li_4GeS_4$, respectively), as stoichiometric $Li_2S$ and $Li_4GeS_4$ do not show significant Li diffusion and a converged AIMD simulation requires a much longer simulation time.

## References


43. Ong, S. P. *et al.* Python materials genomics (pymatgen): A robust, open-source python library for materials analysis. *Comput. Mater. Sci.* **68**, 314–319 (2013).
44. Momma, K. & Izumi, F. VESTA 3 for three-dimensional visualization of crystal, volumetric and morphology data. *J. Appl. Crystallogr.* **44**, 1272–1276 (2011).
45. Perdew, J. P., Burke, K. & Ernzerhof, M. Generalized gradient approximation made simple. *Phys. Rev. Lett.* **77**, 3865–3868 (1996).
46. Blöchl, P. E. Projector augmented-wave method. *Phys. Rev. B* **50**, 17953–17979 (1994).
47. Kresse, G. Efficient iterative schemes for *ab initio* total-energy calculations using a plane-wave basis set. *Phys. Rev. B* **54**, 11169–11186 (1996).
48. Henkelman, G., Uberuaga, B. P. & Jónsson, H. A climbing image nudged elastic band method for finding saddle points and minimum energy paths. *J. Chem. Phys.* **113**, 9901–9904 (2000).